High-Frequency Harmonic Loss Location Verification Using Temperature Rise

Lípa Miroslav, Tiihonen Matias, Kärkkäinen Hannu, Nerg Janne, Aarniovuori Lassi

DOI: 10.1109/IEMDC60492.2025.11061066

High-Frequency Harmonic Loss Location Verification Using Temperature Rise

Miroslav Lípa
Electrical Drives Technology
LUT University
Lappeenranta, Finland
miroslav.lipa@lut.fi

Matias Tiihonen
Electrical Drives Technology
LUT University
Lappeenranta, Finland
matias.tiihonen@lut.fi

Hannu Kärkkäinen
Electrical Drives Technology
LUT University
Lappeenranta, Finland
hannu.s.karkkainen@lut.fi

Janne Nerg
Electrical Drives Technology
LUT University
Lappeenranta, Finland
janne.nerg@lut.fi

Lassi Aarniovuori
Electrical Drives Technology
LUT University
Lappeenranta, Finland
lassi.aarnivuori@lut.fi

***Abstract*—The additional high-frequency harmonic losses in the stator of an electrical machine are a consequence of pulse-width modulation (PWM). These losses are mainly due to the added harmonics from the PWM supply, which increases the eddy current and hysteresis losses in the iron sheets. In this paper, high-frequency harmonic losses are studied using a specially constructed 5-kW, four-pole squirrel cage induction machine equipped with 18 Pt-100 sensors. To enable observation of differences in local temperature rise, the same operating points of the motor are measured for generator supply providing a sinusoidal voltage and for converter supply. These findings are further supported by a complementary simulation in which the same motor is modeled using the finite element method (FEM) for both power supply configurations. The differences in temperature rise can be directly used to indicate the location of the increased losses due to PWM supply. In addition, the harmonic power of the supply waveforms recorded in the experimental tests with different switching frequencies are extracted and compared with the temperature rises to verify the loss increase. It is found that the losses behave similarly to the increase in temperature, thus confirming their correctness.**

***Index Terms*—Harmonic loss measurements, sinusoidal-PWM supply comparison, converter-fed induction motor, temperature sensors, PWM, finite element method,**

I. Introduction

Converter-fed induction motors are recognized as globally efficient solutions for variable-speed applications, primarily because PWM allows for both amplitude and frequency control of the stator voltage. This capability offers advantages such as flexible speed control and high efficiency, but it also brings certain disadvantages, including higher losses due to harmonic components in the PWM-induced distorted voltage waveforms [1]. These harmonic losses appear in both the winding and the motor core [2], increasing all the main loss components of the machine [3].

Despite the widespread use of PWM supply, the harmonic losses remain incompletely described [1]. Moreover, the losses are influenced by multiple factors, including operating speed, the number of pole pairs, motor design, and PWM characteristics such as switching frequency and modulation type [4]. Their modeling thus becomes complex [5] and is often approximated as a percentage of total motor loss. At lower operating points with reduced load, harmonic losses can attain half of total losses [5], contributing to vibration, noise, and motor overheating. If the temperature becomes too high, the heat degrades the insulation and the motor requires additional cooling measures [6]. Furthermore, PWM modulation introduces high voltage spikes that stress conductors and insulation, reducing the operational lifespan of the machine [7]. Harmonic losses tend to be most pronounced in large or high-speed motors, reaching up to one-third of total losses at higher speeds. They are also influenced by flux saturation. Higher flux densities may reduce the variation in flux from high-frequency harmonics, so more saturated machines can exhibit lower harmonic losses [8]. Various PWM modulation methods can be used to create quasi-sinusoidal voltages at different speeds, but decisive conclusions regarding which technique is optimal for lowest harmonic losses have not yet been drawn, and the best modulation approach remains unclear [9].

Two primary approaches are used to estimate harmonic losses: experimental measurement and simulation. In experimental settings, both direct and indirect measurement methods are used. The IEC 60034-2-1 standard and more specifically the IEC 60034-2-3 standard provide guidelines for determining efficiency and losses in converter-fed machines [10], [11]. IEC 60034-2-3 describes a number of determination methods, with direct input-output measurement being the main method. However, while the input-output method evaluates the total power balance and is useful for efficiency determination, it does not isolate the high-frequency harmonic losses. Furthermore, direct methods are susceptible to uncertainties, particularly under PWM operation [12], due to the complexity of separating harmonic-related losses from total losses. In addition to direct measurement methods, the IEC 60034-2-3

standard also describes an indirect method, called summation of losses, which segregates specific loss components. The loss segregation has been validated with high precision for a single machine [13]. Another indirect method for loss measurement is calorimetry. This approach can provide highly accurate total loss measurements, but requires long testing durations, stable environmental conditions, and skilled personnel [14].

Different experimental techniques for direct PWM loss measurement have been proposed in various studies. For example, a method utilizing harmonic injection, where a specific harmonic is introduced into the supply waveform, for example, the PWM waveform [15], and comparative evaluation, which assesses losses by comparing different power supplies [16]. Additionally, frequency domain analyses have been explored as a possible way to separate harmonic components from motor input power [5], as well as impedance-based loss estimation techniques [16]. Although these methods promise accurate results within their own limitations, they have not been widely adopted and thus remain at the experimental stage. Furthermore, it is important to note that the variable speed nature of PWM drives requires testing at multiple operating points, and it is not possible to rely on a single-speed evaluation [17].

When using simulation methods, finite element analysis (FEA) has become a standard approach for estimating harmonic losses and predicting transient effects of PWM voltage on induction motors. Although FEA is widely used for electrical machine calculations, often in a Cartesian 2D setup that captures the start of the motor [1], it should be noted that FEA requires careful selection of the time step size and mesh density, especially when modeling high-frequency harmonics [1]. Alternatives to FEA include analytical evaluations in tools like MATLAB, which can quickly assess losses [18], [19], but often do not account for operating temperatures or motor slip changes [18]. In induction motor modeling, the slip itself is a challenge. In many simulations it is fixed, whereas in real machines it varies with temperature and rotor resistance [20]. Even advanced iron loss models that incorporate hysteresis coefficients [19] may not capture the key added losses from the PWM harmonic power [18].

In this study, PWM-induced harmonic losses in a converter-fed induction motor were analyzed using FEA simulations and experimental measurements. Harmonic loss locations were identified by examining temperature rise differences for different motor components. In addition, the effect of switching frequency on harmonic losses was also investigated. The simulations aimed to replicate the electromagnetic characteristics of the motor accurately and to assess the impact of the PWM supply on the harmonic losses. The simulation methodology is detailed in the following section II, and the experimental measurements are discussed in the section III. This study is derived from the first author's master's thesis [21].

II. FEM SIMULATION OF MACHINE

The rated conditions of the induction machine considered in the study are specified in Table I.

TABLE I
RATED VALUES OF THE TESTED MACHINE

U_n **[V]**	P_n **[kW]**	f **[Hz]**	n **[rpm]**
400	5	50	1450
T **[Nm]**	I_n **[A]**	η **-**	λ **-**
32.9	10.4	0.89	0.74

The machine is supplied with a line-to-line voltage U_n and has a rated output power P_n with rated torque T and rated current I_n. The supply frequency is f with a corresponding rated speed n. The efficiency is described by η and λ the power factor.

The converter-fed induction machine was tested and analyzed. ANSYS MAXWELL, an FEA software, was used to model an induction machine with a squirrel cage. The electrical machine design tool RMXprt was used for model generation. The induction motor is fitted with a squirrel cage with 40 aluminum rotor bars and 48 stator slots.

The simulations were matched with the measured data. For simulation of the PWM supply, the voltage waveforms of the motor were captured during the machine testing phase with a converter supply. To accurately simulate such supply, the method employed involved reconstructing the voltage equations, which were subsequently implemented as a source within the FEM software. Derivation of the voltage equations was conducted through analysis of these waveforms using MATLAB. Equation (1) shows the general formula for voltage:

$$u(t) = \sum_{n=1}^{N} U_n \cos(n\omega t + \theta_n), \tag{1}$$

where the voltage $u(t)$ is expressed as the contributions from multiple harmonics. The amplitude of the nth harmonic is represented by U_n (this is not the line-to-line voltage from previous Table I), while n denotes the harmonic order. The angular frequency of the fundamental component is given by ω. Each harmonic component has an associated phase angle θ_n. The total number of harmonics considered in the summation is represented by N.

Due to the inherent characteristics of the PWM supply, the number of harmonics is considerable, posing challenges for formulation of a comprehensive equation and accurate representation of the voltage waveform. Before applying Fast Fourier Transform (FFT) on the waveform, it had to be filtered and limited to reduce noise and the number of harmonics. To address a large spectrum of harmonics, it was necessary to limit the harmonic spectrum by setting a minimum threshold of 5 % of the first harmonic amplitude value, which was around 291 V for the first load point with rated torque and 90 % rated speed. The 5 % limit was carefully chosen to include as many harmonics as possible, while still allowing the voltage equation to be accurately inserted into the FEA software as the source voltage. The raw voltage waveform, the filtered waveform with two filters and the limited twice filtered waveform are shown in Fig. 1. With prefiltering, the noise was reduced, and the second

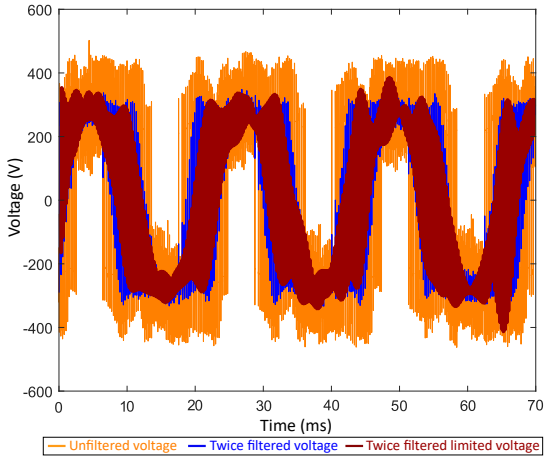

Fig. 1. Comparison of original recorded voltage waveform with twice filtered voltage waveform and twice filtered limited waveform. Filters remove noise and reduce the size of the frequency spectrum. The recorded voltage waveform is obtained from measurement of phase A for the first load point with rated torque and 90 % speed. Effect of filtered noise and reduced spectrum can be seen in the orange waveform and effect of adding the 5 % limit to it is shown in the dark red waveform.

filter serves to reduce the size of the spectrum. In addition, the phase shifts of the harmonics were analyzed to ensure proper waveform reconstruction. Fig. 2 illustrates the filtered harmonic spectrum of the voltage used for the simulations. All three phases were analyzed, which revealed approximately 25 harmonics in the spectrum per phase. Most of these harmonics were concentrated around the switching frequency, as seen in Fig. 2.

For comparison, Fig. 3 shows three plots of the cumulative power: namely, cumulative power for the recorded unfiltered voltage waveform in Fig. 1, the voltage waveform prefiltered with a Butterworth 10 kHz filter without noise, and the limited twice filtered voltage waveform in Fig. 1, respectively. The power difference between the filtered waveform and the other two waveforms remains relatively small, indicating that a

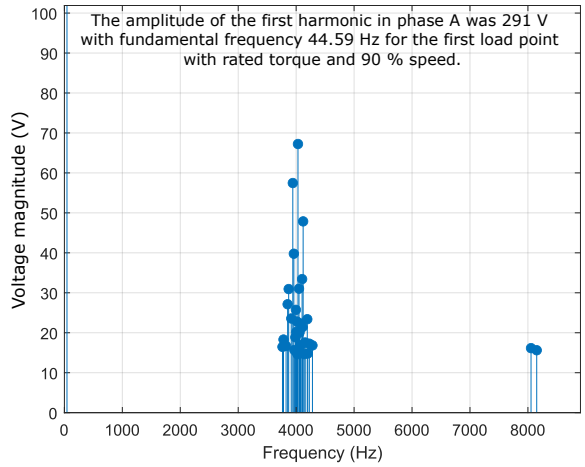

Fig. 2. Filtered single-sided amplitude spectrum voltage. Figure shows limited harmonics used for remodeling of PWM supply in the finite element method. The harmonic spectrum was obtained using the measured voltage of phase A at the load point with rated torque and 90 % speed. The amplitude of the first harmonic was 291 V, for easier readability it is scaled out.

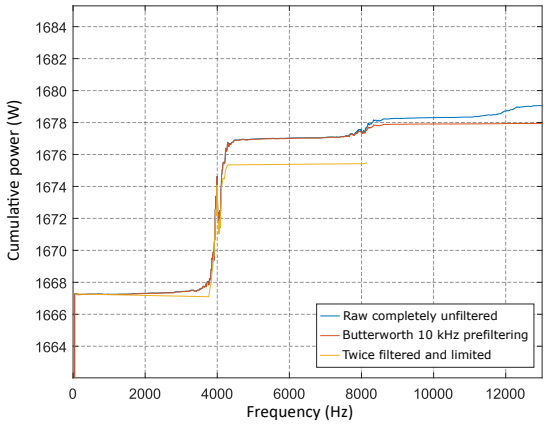

Fig. 3. Comparison of cumulative power for different filtered voltage waveforms. The curves are results obtained using the measured power of phase A at the load point with rated torque and 90 % speed with filters and limit. The cumulative power values show input power of phase A without filter, with filter and with filters and limit. The input power was around 5 kW.

certain level of compromise has been achieved. Compromise in this context refers to maintaining a similar input power for a machine while using filters and limits to minimize harmonics so the modeling of PWM source would be doable. The cumulative power that goes into phases grows with bigger frequency spectrum because of additional harmonics.

The next section considers the effect of PWM on the current wave. Fig. 4 presents the waveform for PWM supply simulated using the filtered waveform. Currents are shown for the simulation of the first load point with the rated torque and 90 % speed. Compared to the classic smooth current sinusoidal wave from a sinusoidal generator voltage supply, Fig. 4 shows the effect of introduced harmonics through PWM analysis in the current waveform. These harmonics were added to the simulation through modified voltage equations that were created based on the harmonics in Fig. 2.

Table II presents the measured and simulated results for PWM and sinusoidal supplies and Table III provides percentage differences of the simulated values compared to the measured values. Results are shown for the first load point P1

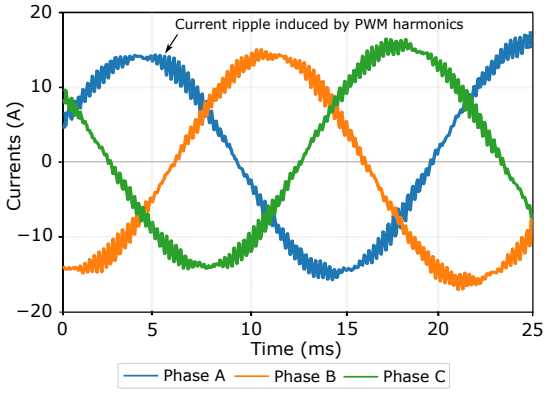

Fig. 4. Current waveform in steady state for PWM supply simulated using the filtered waveform with reduced harmonics. The figure shows all three phases simulated for first load point with rated torque and 90 % speed. Each phase has its own induced current ripple from the PWM. With the fundamental frequency 44.59 Hz, the period of the waveform is 22.42 ms.

TABLE II
MEASURED AND SIMULATED RESULTS FOR PWM AND SINUSOIDAL SUPPLIES

Quantity	PWM Meas.	PWM Sim.	SINE Meas.	SINE Sim.
I_n (A)	10.4	10.7	10.4	10.5
P_1 (W)	5032.1	5140.5	4981.7	4960.5
S (VA)	8126.0	7764.4	6411.6	6475.0
Q (VAr)	6380.4	5819.4	4036.2	4162.4
λ	0.62	0.66	0.78	0.77
P_n (W)	4502.0	4526.4	4501.5	4520.7
n (rpm)	1305.7	1301.9	1306.5	1302.1
T (Nm)	32.9	33.2	32.9	33.0
P_{loss} (W)	530.1	685.9	476.5	605.7
η (%)	89.5	88.1	90.4	90.8

TABLE III
RELATIVE DIFFERENCE OF SIMULATED RESULTS COMPARED TO MEASURED VALUES FOR PWM AND SINUSOIDAL SUPPLIES

Quantity	Rel. increase for PWM (%)	Rel. increase for SINE (%)
I_n	2.9	1.0
P_1	2.1	-0.4
S	-4.7	0.1
Q	-9.7	3.0
λ	6.2	-1.4
P_n	0.5	-0.1
n	-0.4	-0.3
T	0.8	0.3
P_{loss}	22.7	21.3
η	-1.7	0.4

(rated torque, 90 % speed). It can be seen from Table III that there are clear similarities in the behavior of the simulation and the experimental measurements. The relative differences observed with the generator supply are significantly lower and align closely with the measured values. However, the total loss difference remains substantial and comparable to that observed in the PWM comparison. This suggests that the loss model may not have been configured wholly accurately.

The symbols in the table represent; rated current I_n, input power P_1, apparent power S, reactive power Q, rated output power P_n, torque T, rotational speed n, power factor λ, total losses P_{loss} and efficiency η.

III. EXPERIMENTS WITH CONVERTER AND GENERATOR SUPPLY

A timetable, was established for the experimental measurements that divided the measurements into several parts. Following EN IEC 60034-2-3 [10] recommendations, the induction motor was loaded with seven standardized operating points with two different power supplies. The operating points are shown in Fig. 5.

The motor was placed in a chamber that maintains constant ambient conditions. The operating temperature of the chamber was 27 °C. The temperature in the chamber is maintained by a heating resistor and controlled to the predetermined temperature using the LabVIEW interface. Several temperature sensors in the chamber sense the temperature at specific locations, thus enabling accurate temperature control. 18 PT-100 sensors are installed in the induction motor. Sensors within the stator slots are evenly distributed along the depth of the motor. Additional sensors are strategically positioned at both

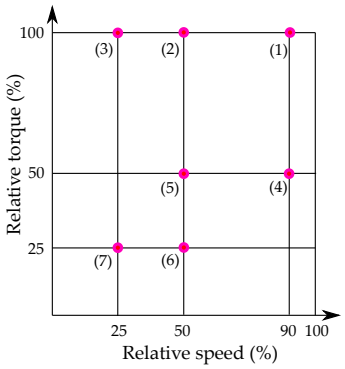

Fig. 5. Standardized loading points from EN IEC 60034-2-3 [10]. These points were used for experimental measurements. The order used for measurements was as they are marked in the figure from (1) to (7), with the first point being with rated torque and 90 % speed and last point with 25 % torque and 25 % speed.

the drive end and non-drive end, embedded in the stator core and in the end windings. Sensors are additionally installed within the rotor: one in the rotor yoke and the other in the end ring. The rotor sensors use wireless signal transfer. The locations of the temperature sensors are shown in Fig. 6.

A load in the form of a second electric motor was connected to the tested induction motor. The load is controlled by its own frequency converter. A measuring shaft connected before the load measures the machine speed and torque on the shaft. The final component is the power analyzer, which measures the electrical parameters of the machine. All measured parameters are displayed through the LabVIEW interface, allowing for sequential recording and monitoring of the entire measurement process. Standard bearings were used to couple the load, the measuring shaft, and the machine being tested. The torque readings included the bearing offset, which had to be taken into account when adjusting the load. For easier understanding, the measurement methodology is presented in block diagram form in Fig. 7.

A preliminary assessment involved conducting a retardation test to estimate mechanical losses. The retardation curve ranged from 3500 rotations per minute, and several retardation curves were measured while cooling down. Additionally, the temperature dependence of the mechanical losses was verified by using multiple measured curves. Mechanical losses were not dependent on temperature.

Mechanical losses for varied speeds can be obtained from

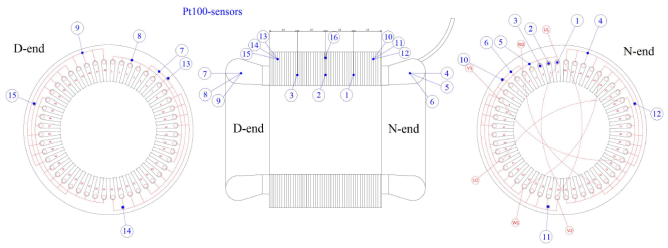

Fig. 6. Placement of the PT-100 temperature sensors. Sensors are placed in the groups that create for major parts. The groups are stator winding, stator iron, rotor yoke and rotor end ring. All the temperature data are collected using these temperature sensors.

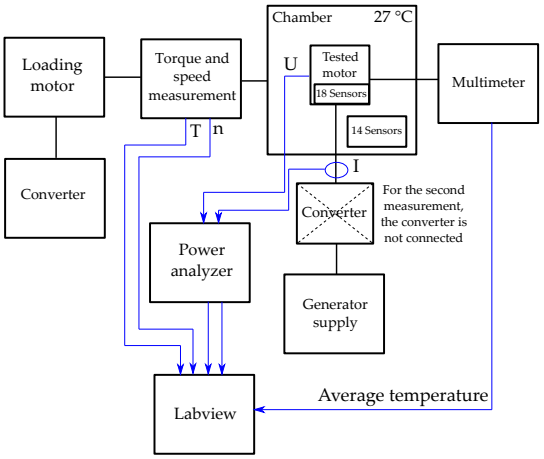

Fig. 7. Measurement block diagram. The figure shows the 18 temperature sensors located in the tested motor and also 14 temperature sensors located in the chamber to keep the temperature at 27°C. In the diagram, the converter connected to the test machine was supplied by the generator and used for the PWM measurements and later was disconnected for just the sinusoidal supply measurements.

Fig. 8. Tab. IV shows the retardation test values for the nominal point calculated using MATLAB code. The results were later used in the FEA simulations and model.

After a retardation test aimed at quantifying mechanical losses, the motor was powered by a frequency converter that used four different carrier frequencies while maintaining the same load condition, i.e. load point P2 (50 % speed, rated torque) from Fig. 5. The aim was to observe the increase in total loss due to harmonics as a function of carrier frequency. The motor was run with each carrier frequency until thermal equilibrium before the recordings were taken. The temperature rise shown in Fig. 9 verifies the increase in total loss.

At lower carrier frequencies, specifically between 2 kHz and 4 kHz, the reduction in total motor losses is significant;

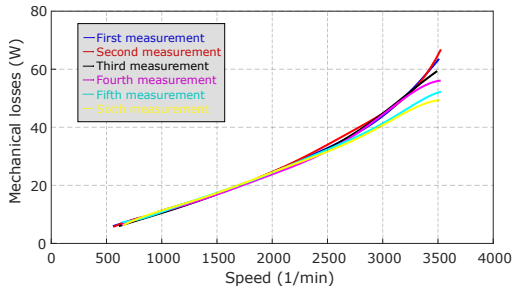

Fig. 8. Retardation curves presenting mechanical losses versus speed. There were six measurements in total to examine if the curves are temperature dependent. The final value of the mechanical losses was a average of all six curves.

TABLE IV
RETARDATION TEST RESULTS FOR SPECIFIC SPEED WITH INERTIA INFORMATION.

Category (Unit)	Value
Friction and windage loss at 1450 rpm (W)	16.63
Calculated motor inertia (kg·m^2)	0.029
Inertia of bearings (kg·m^2)	0.00343

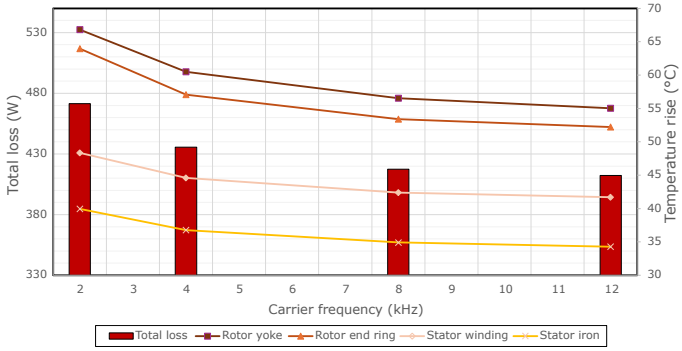

Fig. 9. Comparison of total losses and temperature rise for different carrier frequencies. The red bars are representing total loss at specific carrier frequencies and are compared with temperature rise curves with data from temperature sensor groups mentioned in the Fig. 6.

however, at higher frequencies, the difference in motor losses between different frequencies decreases considerably.

After completing this measurement, the next phase involved assessing additional operating points, for which a carrier frequency of 4 kHz was selected. Measurements were taken every day at the same local time. This method was chosen because of the variable conditions in the laboratory. Although the chamber air temperature at the inlet was controlled and stable, there was some variability in the inside temperature depending on the time of day. The third measurement focused on using a standard sinusoidal waveform provided by a generator. Electrical parameters such as fundamental voltage and fundamental frequency were accurately replicated in all 7 test points, which ensured that the measurements with the sinusoidal source were comparable with the converter measurements. A comparison of the total losses and average temperature rise of the motor is presented in Fig. 10.

The apparent linear trend arises from variations in the losses associated with this machine at different operating points, which are largely coincidental. Losses and increase in temperature in an electrical machine are expected to exhibit a proportional relationship. Thus, PWM supply results in higher total losses and higher temperature rises compared to

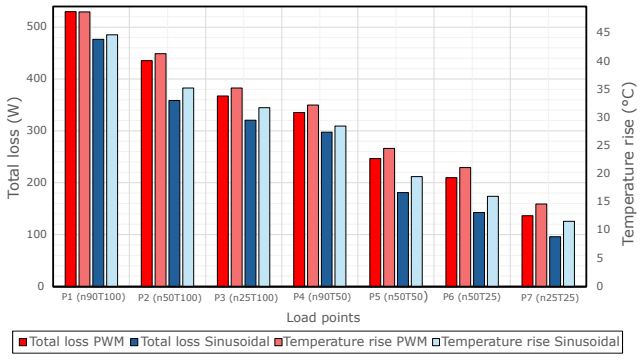

Fig. 10. Comparison of total losses and temperature rise for different load points with PWM source and sinusoidal source. The dark red and blue represent the total loss for both the supplies and light red and blue show the temperature rise for both the supplies. The notation inside brackets after each load point number gives the speed and toque percentages, e.g n90T100 refers to 90 % speed and 100 % torque.

sinusoidal supply at all load points. From Fig. 10 it can be seen that at the first operating point, the use of PWM supply increases the total losses by 11 % and the temperature rises by 9 %. The most significant relative increases in both total losses and temperature increase are observed at loading points where there is 50 % of the rated rotational speed of the machine. This effect is particularly pronounced at Loading Point 6, where the rated rotational speed is 50 %, and the load corresponds to only 25 % of the rated torque. Under these conditions, the motor shows the most significant change, with total losses increasing by 47 % and temperature increasing by 32 %. This phenomenon is attributed to a square-wave voltage with a modulation index of approximately 0.5, which leads to the highest current ripple.

Fig. 11 gives insights into the measured temperature rise differences and the total loss differences between the motor parts. In addition, the calculated fundamental rotor losses from slip values and the airgap power are shown in Fig. 12. These losses do not represent the total loss of the rotor. The results show that higher supply frequencies tend to produce larger variations in total loss and temperature difference, and lower frequency has relatively stable and lower loss differences and temperature rise differences. The total loss difference and temperature rise difference increase with load, with the exception that at 50 % speed the lowest values are at 50 % load. This behaviour could be explained by different frequency fractions in the motor. The total losses behave similarly with increasing temperature, confirming that the losses are correct. The loss increase is highest with 50 % speed. The results also indicate that the rotor losses increase more than the stator losses when the machine is supplied from the PWM supply, which is a finding supported by the values in Fig. 12. Moreover, a slight increase in fundamental rotor losses between the PWM supply and the sinusoidal supply can be noted, which might be explained by the higher temperature of the rotor cage and its higher resistance.

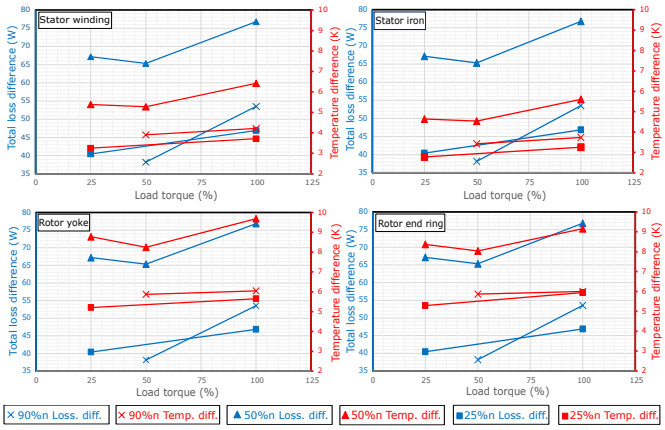

Fig. 11. Comparison of temperature rise difference and loss differences in four parts of the motor between sinusoidal supply and PWM supply. The blue characteristics represent total loss difference and red characteristics represent total temperature difference between supplies. The special symbols in the legend of this figure are used to define different speeds. The parts of the motor are groups of temperature sensors explained in Fig. 6.

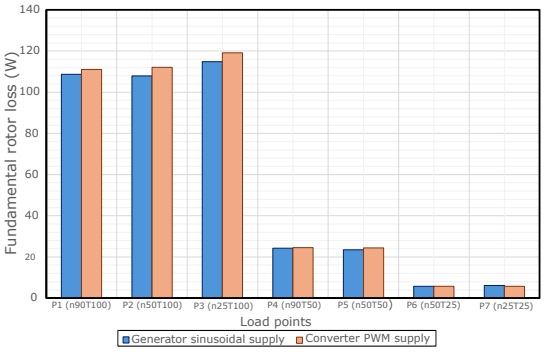

Fig. 12. Fundamental rotor loss for different supply types. The blue bars represent the fundamental rotor loss with sinusoidal supply and red bars represent the fundamental rotor loss with PWM supply for all seven loading points explained in Fig. 5. The fundamental rotor loss values does not show the total rotor loss value.

Discussion

The results of the FEA model confirm that the electromagnetic properties of the motor were accurately replicated, as can be seen by comparing the simulated and measured results in Table II and Table III. Additionally, the results show similarity in relative trends. Although the total losses demonstrate significant differences, relative trends remain consistent, suggesting that the loss model may require further tuning to improve accuracy. Notably, for the first load point, the relative increase in harmonic losses aligns well with the experimental data, whereas this consistency is not observed across all load points. Future efforts should focus on optimizing the model parameters to improve the accuracy of loss calculations for all operating conditions. The voltage waveform was reconstructed for the PWM supply and the effect of PWM on the current waveforms is illustrated in Fig. 4, where the PWM supply waveform exhibits clear harmonic components.

The effect of carrier frequency on total losses is evident in Fig. 9. Higher carrier frequencies lead to a reduction in the total losses and a corresponding reduction in temperature rise. The most significant improvement is observed when the frequency is increased from 2 to 4 kHz. Beyond this point, however, the effect of loss reduction decreases, suggesting that higher switching frequencies might yield diminishing returns, since higher switching frequencies increase bridge losses in the converter. Thus, the trade-off between switching and conduction losses must be optimized. These results further support the theory that the voltage waveform is highly distorted at lower switching frequencies, resulting in higher losses compared to higher switching frequencies, confirming findings in [1], [2], [3], and [22].

The dependence of total losses and temperature rise on both frequency and load is illustrated in Fig. 10. Across all load points, PWM excitation consistently resulted in higher total losses and higher temperature rise compared to sinusoidal excitation. The greatest increase in losses was observed at lower rotational speeds (supply frequencies) and lower load conditions. For Load Point 6 (50 % rated speed and 25 % rated load), total losses increased by 47 %, while the temperature

rise increased by 32 %. At half-speed conditions, the square-wave voltage has a modulation index of approximately 0.5, leading to excessive current ripple.

An essential innovative aspect of the study was the use of temperature sensors to assess the localized heating within the motor. Fig. 11 provides a detailed breakdown of temperature rise and loss distribution between different motor components, highlighting that the rotor is the region most affected. This observation correlates with values in Fig. 12, where the fundamental losses of the rotor were calculated based on the slip and air gap power. Furthermore, the results indicate that the losses of the rotor are higher under PWM supply than sinusoidal supply, suggesting that a more optimized rotor structure could improve performance under PWM operation. In future work, a thermal model is to be created to analyze where and in which kind of proportions the additional PWM supply caused losses to occur in the motor parts.

CONCLUSIONS

Temperature rise is a reliable indicator of losses and the research carried out here supports earlier studies. While the trend to utilize wide band gap devices might decrease interest in high frequency harmonics losses in some small power applications, it can be expected that silicon based IGBTs will be used in high power or high voltage applications for many decades yet. High-frequency PWM-induced losses are the only major loss component that cannot yet be reliably modeled. Research, however, shows that these losses can be measured and segregated using experimental testing. Nevertheless, the overall uncertainty of observed PWM losses is significant, although temperature measurements can aid in verification. The same methods can be used to assess harmonic losses when IGBTs or other silicon based devices are employed. High-switching-frequency wide band gap devices significantly minimize harmonic losses in motor drives, but they also introduce additional issues (insulation, EMC, etc.)

REFERENCES

[1] M. Zaheer, P. Lindh, L. Aarniovuori, and J. Pyrhönen, "Converter-fed induction motor finite element analysis with different time steps," in *2020 XI International Conference on Electrical Power Drive Systems (ICEPDS)*, 2020, pp. 1–7.

[2] Z. Gmyrek, A. Boglietti, and A. Cavagnino, "No-load loss separation in induction motors operated by pwm inverters: Numerical and experimental approaches," in *IECON 2011 - 37th Annual Conference of the IEEE Industrial Electronics Society*, 2011, pp. 1941–1947.

[3] D. Zhang, J. Shi, H. Zhao, and T. Wu, "Loss characteristic analysis of small and medium-sized induction motors fed by pwm inverter based on the experiment measurements," in *IECON 2017 - 43rd Annual Conference of the IEEE Industrial Electronics Society*, 2017, pp. 2053–2058.

[4] *Rotating electrical machines - Part 25: AC electrical machines used in power drive systems - Application guide*, International Electrotechnical Commission Std. IEC Technical Specification 60 034-25, Rev. 4.0, June 2022.

[5] H. Kärkkäinen, L. Aarniovuori, S. Makkonen, M. Niemelä, and J. Pyrhönen, "Determination of high-frequency harmonic power in converter-fed motors," in *2022 International Conference on Electrical Machines (ICEM)*, 2022, pp. 394–400.

[6] A. Strandt, J. Hu, and L. Wei, "No-load power losses and motor overheating effects versus pwm switching frequencies," in *2014 International Conference on Renewable Energy Research and Application (ICRERA)*, 2014, pp. 280–283.

[7] G. Suresh, H. Toliyat, D. Rendusara, and P. Enjeti, "Predicting the transient effects of pwm voltage waveform on the stator windings of random wound induction motors," *IEEE Transactions on Power Electronics*, vol. 14, no. 1, pp. 23–30, 1999.

[8] A. Boglietti, A. Cavagnino, A. M. Knight, and Y. Zhan, "Factors affecting losses in induction motors with non-sinusoidal supply," in *2007 IEEE Industry Applications Annual Meeting*, 2007, pp. 1193–1199.

[9] L. Aarniovuori, H. Kärkkäinen, M. Niemelä, and J. Pyrhönen, "Pwm power distribution and switching frequency analysis in motor drives," in *IECON 2016 - 42nd Annual Conference of the IEEE Industrial Electronics Society*, 2016, pp. 4356–4361.

[10] *Rotating electrical machines - Part 2-3: Specific test methods for determining losses and efficiency of converter-fed AC motors*, International Electrotechnical Commission Std. IEC 60 034-2-3, Rev. 2.0, March 2024.

[11] *Rotating electrical machines - Part 2-1: Standard methods for determining losses and efficiency from tests (excluding machines for traction vehicles)*, International Electrotechnical Commission Std. IEC 60 034-2-1, Rev. 3.0, March 2024.

[12] H. Kärkkäinen, L. Aarniovuori, M. Niemelä, and J. Pyrhönen, "Advanced uncertainty calculation method for converter-fed motor loss determining," in *2019 IEEE International Electric Machines & Drives Conference (IEMDC)*, 2019, pp. 1551–1558.

[13] L. Aarniovuori, P. Rasilo, M. Niemelä, and J. J. Pyrhönen, "Analysis of 37-kw converter-fed induction motor losses," *IEEE Transactions on Industrial Electronics*, vol. 63, no. 9, pp. 5357–5365, 2016.

[14] L. Aarniovuori, H. Kärkkäinen, A. Kosonen, J. Pyrhönen, Z. Liu, and W. Cao, "Overview of calorimetric systems used in loss determination of electric motors and drives," in *IECON 2017 - 43rd Annual Conference of the IEEE Industrial Electronics Society*, 2017, pp. 2110–2115.

[15] K. Bradley, W. Cao, J. Clare, and P. Wheeler, "Predicting inverter-induced harmonic loss by improved harmonic injection," *IEEE Transactions on Power Electronics*, vol. 23, no. 5, pp. 2619–2624, 2008.

[16] D. Cittanti, V. Mallemaci, F. Mandrile, S. Rubino, R. Bojoi, and A. Boglietti, "Pwm-induced losses in electrical machines: An impedance-based estimation method," in *2021 24th International Conference on Electrical Machines and Systems (ICEMS)*, 2021, pp. 548–553.

[17] L. Aarniovuori, H. Kärkkäinen, M. Niemelä, K. Cai, J. Pyrhönen, and W. Cao, "Experimental investigation of the losses and efficiency of 75 kw induction motor drive system," in *IECON 2019 - 45th Annual Conference of the IEEE Industrial Electronics Society*, vol. 1, 2019, pp. 1052–1058.

[18] S. Khalghani, L. Aarniovuori, and J. Pyrhönen, "Evaluation of 5 kw converter-fed induction motor losses by analytical calculation," in *2022 29th International Workshop on Electric Drives: Advances in Power Electronics for Electric Drives (IWED)*, 2022, pp. 1–6.

[19] S. Xue, J. Feng, S. Guo, Z. Chen, J. Peng, W. Q. Chu, P. L. Xu, and Z. Q. Zhu, "Iron loss model for electrical machine fed by low switching frequency inverter," *IEEE Transactions on Magnetics*, vol. 53, no. 11, pp. 1–4, 2017.

[20] L. Aarniovuori, P. Lindh, H. Kärkkäinen, M. Niemelä, J. Pyrhönen, and W. Cao, "Analytical evaluation of high-efficiency induction motor losses," in *2019 IEEE International Electric Machines & Drives Conference (IEMDC)*, 2019, pp. 1501–1507.

[21] M. Lípa, "Losses in induction machines supplied by a frequency converter," Master's thesis, Brno University of Technology, Faculty of Electrical Engineering and Communication, Department of Power Electrical and Electronic engineering, 2024.

[22] E. Nicol Hildebrand and H. Roehrdanz, "Losses in three-phase induction machines fed by pwm converter," *IEEE Transactions on Energy Conversion*, vol. 16, no. 3, pp. 228–233, 2001.